Nanoscale

Long-lived luminescence of colloidal silicon quantum dots for time-gated fluorescence imaging in the second near infrared window in biological tissue

Journal:	*Nanoscale*
Manuscript ID	NR-COM-05-2018-003571.R1
Article Type:	Communication
Date Submitted by the Author:	06-Jun-2018
Complete List of Authors:	Sakiyama, Makoto; Kobe University, Department of Electrical and Electronic Engineering Sugimoto, Hiroshi; Kobe University, Department of Electrical and Electronic Engineering Fujii, Minoru; Kobe University, Department of Electrical and Electronic Engineering, Graduate School of Engineering

Journal Name

COMMUNICATION

Long-lived luminescence of colloidal silicon quantum dots for time-gated fluorescence imaging in the second near infrared window in biological tissue

Received 00th January 20xx,
Accepted 00th January 20xx

DOI: 10.1039/x0xx00000x

www.rsc.org/

Makoto Sakiyama [a], Hiroshi Sugimoto [a†], and Minoru Fujii [a†]

Boron (B) and phosphorus (P) codoped silicon quantum dots (Si QDs) are dispersible in polar solvents without organic ligands and exhibit the photoluminescence (PL) is the first (NIR-I) and second (NIR-II) near infrared (NIR) windows in biological tissues due to the optical transition from the donor to acceptor states. We study the relation between the PL wavelength, lifetime and QY of the colloidal solution and the composition of the starting material for the preparation. We found that the PL lifetime and the quantum yield (QY) are primarily determined by the composition, while the PL wavelength is mainly determined by the growth temperature. By optimizing the composition, we achieve the QYs of 20.1 % and 1.74 % in the NIR-I and NIR-II regions, respectively, in methanol. We demonstrate the application for time-gated imaging in the NIR-II range.

Fluorescence bioimaging is a versatile tool in biomedical research, especially for clinical diagnostics, because of the easy and fine visualization of the region of interest.[1] Fluorescence imaging in the near-infrared (NIR) wavelength range has several advantages compared to visible imaging such as weaker autofluorescence of bio-substances and the smaller scattering and absorption. In the past decade, the development of the NIR fluorescence imaging technique has focused on the traditional 700-950 nm NIR window (NIR-I) due to the high availability of organic phosphors with high photoluminescence (PL) quantum yield (QY)[2–6] and high sensitive CCD detectors. Recently, the wavelength range has been extended to the second NIR window (NIR-II, 1000–1700 nm). In the NIR-II window, tissue scattering and autofluorescence are further reduced, which makes probing tissues at cm depths with high spatial resolution possible.[7]

A problem of the NIR-II fluorescence imaging is the lack of proper phosphors usable for practical clinical diagnostics, although the development has been accelerating.[8] Very recently, over 10% QY in the NIR-II window was reported in a molecule-protein complex fluorophore.[9] A possible alternative of organic phosphors for NIR-II bioimaging is semiconductor quantum dots (QDs). The emission wavelength of QDs can be controlled in a wide wavelength range covering the visible to the NIR-II spectral region by controlling the size and the composition. Cadmium (Cd), lead (Pb) and silver (Ag) chalcogenide QDs have been widely studied as biological markers.[10–14] PbS, Ag_2S and Ag_2Se QDs exhibit over 10 % QY in the NIR-II region.[11,12,15,16] Recently, in vivo NIR-II fluorescence imaging of gastrointestinal tract of mice is achieved by QDs composed of a PbS core and a CdS inner shell and a SiO_2 outer shell (PbS@CdS@SiO_2).[17] Similarly, the liver, spleen, and vascular network of mice are visualized in vivo by polymer (poly(maleic anhydride-alt-1-octadecene)-methoxy poly(ethylene glycol) [C18-PMH-PEG]) coated Ag_2Se QDs.[16] Ag_2S QDs functionalized with polyethylene glycol are employed for dynamically labelling and tracking of human mesenchymal stem cells in vivo with high sensitivity and high spatial and temporal resolution.[18]

In addition to these heavy metal chalcogenide QDs, silicon (Si) QDs can be a candidate of a NIR phosphor. Si QDs are known to be highly biocompatible and biodegradable.[19,20] The QY of organic capped Si QDs reaches ~70 % in the NIR-I range,[21,22] although their surface is hydrophobic. Hydrophilic water-dispersible Si QDs have also been developed and NIR-I bioimaging by a Si QDs phosphor has been demonstrated by several groups.[23,24] However, extension of the luminescence wavelength of Si QDs to the NIR-II range is not straightforward. Although a relatively large Si QD (diameter (d) ~ 9 nm) exhibits the luminescence around 1000 nm,[25] further extension of the wavelength to the NIR-II range by increasing the size is not practical due to the relatively large bulk band gap (1.12 eV) compared to Pb and Ag chalcogenides. A possible approach to overcome the problem is introducing in-gap states by impurity doping.[26] It is known that doping boron (B) and phosphorus (P) simultaneously in a Si QD results in the formation of acceptor and donor states in the band gap,[27,28] respectively, which shifts the luminescence energy several hundreds of meV compared

[a] Department of Electrical and Electronic Engineering, Graduate School of Engineering, Kobe University, Rokkodai, Nada, Kobe 657-8501, Japan.
† Corresponding Authors e-mail : sugimoto@eedept.kobe-u.ac.jp
fujii@eedept.kobe-u.ac.jp

to that of an intrinsic Si QD with a comparable size.[29] Therefore, tunable luminescence in the NIR-II range in a Si QD becomes possible by B and P codoping.

An advantage of B and P codoped Si QDs as a phosphor for bioimaging is the high dispersibility in water.[30,31] This is due to the core-shell structure; the core is B and P codoped crystalline Si and the shell is an amorphous hydrophilic layer composed of B, Si and P.[32,33] Therefore, formation of elaborate structures such as PbS@CdS@SiO_2 and/or polymer coating, which are required for Pb and Ag chalcogenide QDs to attain high luminescence QY and high stability in water, is not necessary. This has been demonstrated in the NIR-I range for human monocytes, macrophages, osteoblasts and mesenchymal stem cells.[34,35] Another advantage of codoped Si QDs is the very long luminescence lifetime (~100 μs),[29] which allow us to use time-gated imaging[36,37] in the NIR-II range.

A drawback of codoped Si QDs for bioimaging in the NIR-II window is the relatively small QY (0.14% at 1150 nm).[29] Although the value is comparable to typical fluorescence dye in the same wavelength range (IR-26, QY=0.05% at 1130 nm)[38], it is smaller than that of compound semiconductor QDs. In this paper, we clarify the relation between the doping concentration and the QY and optimize the growth parameter of codoped Si QDs. We show that long-lived luminescence with the QY of above 1% can be achieved in the NIR-II window. The very long lifetime allows us to perform time-gated imaging in the NIR-II window by using a simple mechanical chopping method.

	Sputtering target area (%)				Concentration (at.%)	
	Si	SiO_2	B_2O_3	PSG	B	P
A	6	0	9	85	0.53	0.24
B	6	27	9	58	0.53	0.16
C	6	45	9	40	0.53	0.11
D	6	63	9	22	0.53	0.06
E	6	4.5	4.5	85	0.26	0.24
F	6	31.5	4.5	58	0.26	0.16
G	6	49.5	4.5	40	0.26	0.11
H	6	40	14	40	0.82	0.11
I	6	58	14	22	0.82	0.06

Table 1. List of samples. The areal ratio of the sputtering targets (Si, SiO_2, B_2O_3 and PSG) and B and P concentration in as-grown films are shown. The concentration in sample A is obtained by XPS measurements, while others are estimated from the relation between the concentration and the areal ratio.

B and P codoped Si QDs were prepared by a cosputtering method. Details of the preparation procedure are found in our previous papers.[29,30] Briefly, a thick Si-rich borophosphosilicate glass (BPSG) film (~20 μm in thickness) was deposited on a thin stainless steel plate (100 μm in thickness) by simultaneously sputtering Si, SiO_2, B_2O_3 and phosphosilicate glass (PSG) (SiO_2:P_2O_5=95:5 wt.%). The composition of the film was controlled by the areal ratio of the target materials. In table 1, the target areal ratio of the samples prepared in this work is summarized. In the table, the composition (at.%) of the films are also shown. The composition of sample A is estimated by X-ray photoelectron spectroscopy (XPS) (PHI X-tool, ULVAC-PHI), while that of others are estimated from the relation between the areal ratio and the composition obtained for sample A. After the deposition, a Si-rich BPSG film was peeled off from a thin stainless steel plate by bending the plate and annealed in a N_2 atmosphere for 30 min at 1050, 1075, 1100, 1125, 1150, 1175 or 1200°C. This results in the growth of B and P codoped Si QDs of different sizes in BPSG matrices. Finally, BPSG matrices were removed by hydrofluoric acid (HF) etching (48 wt.%, 30-60 min). Liberated Si QDs were transferred to methanol and stored for more than a month. Hereafter, we distinguish Si QD samples by the symbol in Table 1 and the growth temperature, e.g., A-1200.

For all the samples prepared, absorption spectra, PL spectra, PL decay dynamics and PL QYs were measured. Absorption spectra were measured by a UV-Vis-NIR spectrophotometer (UV-3101PC, Shimadzu). PL spectra were measured by a scanning monochromator equipped with a photomultiplier and a liquid-N_2 cooled InGaAs NIR photodiode (Fluorolog-3, Horiba). Excitation wavelength was 405 nm (monochromatized Xe lamp). PL decay dynamics were measured by a gated intensified charge coupled device (ICCD) (PI-MAX, Princeton Instrument) in a 640-850 nm range and a NIR photomultiplier (R5509-41, Hamamatsu Photonics) in a 710-1240 nm range. The excitation was modulated 405 nm light from a semiconductor laser. The PL quantum yield (QY) was determined by a comparative method.[39]

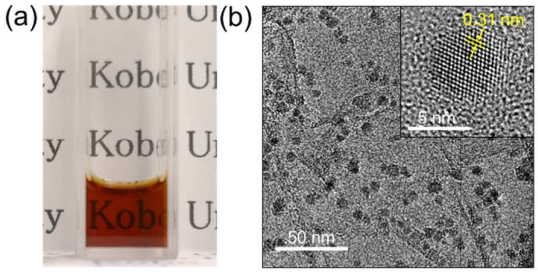

Figure 1. (a) Photograph of a colloidal solution of Si QDs (A-1200). (b) TEM image of A-1200. Inset is the high-relation TEM image of a Si QD.

Figure 1(a) shows a photo of a colloidal solution of A-1200. The solution is perfectly clear and light scattering by agglomerates is not detectable. Figure 1(b) shows a transmission electron microscope (TEM) (JEM-2100F, JEOL) image of A-1200. The sample for the TEM observation is prepared by dropping a diluted solution on a Cu TEM mesh covered by an atomically thin graphene oxide support film. The average diameter of Si QDs estimated from TEM images is 8.3 nm with the standard deviation of 2.0 nm. The inset is the high resolution TEM image of a Si QD. A crossed lattice fringes corresponding to {111} planes of Si crystal (0.31 nm) are clearly seen, indicating the high crystallinity of the QD.

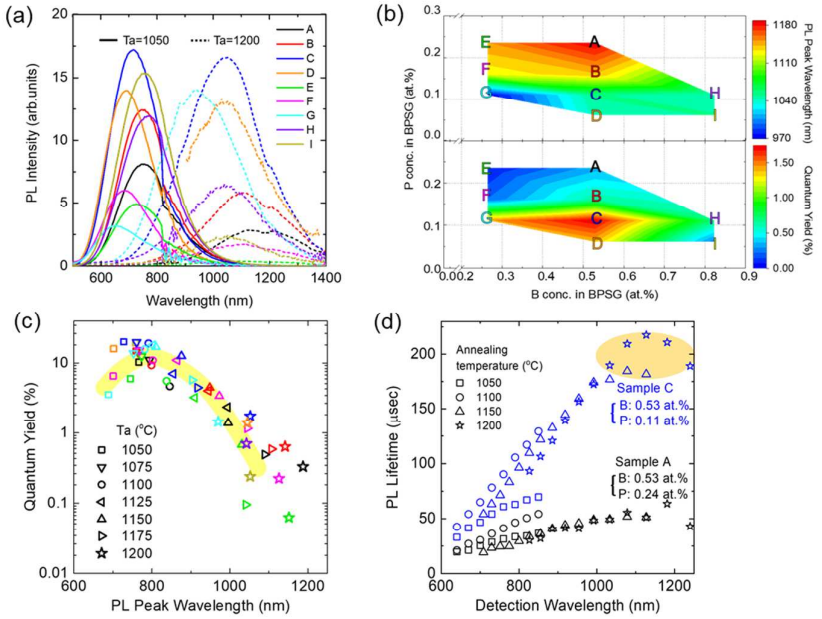

Figure 2. (a) PL spectra of colloidal solution of codoped Si QDs. Symbols A-I correspond to the samples in Table 1. The growth temperatures are 1050 (solid) and 1200°C (dashed). (b) Contour plots of PL peak wavelength (top) and QY (bottom) as a function of B and P concentration. The growth temperature is 1200°C. (c) PL QY as a function of PL peak wavelength. The colour of the symbol is the same as that in (a). The style of the symbols represents the growth temperature (1050-1200°C). (d) PL lifetime as a function of detection wavelength for sample A and C grown at different temperatures. The style of the symbols represents the growth temperature (1050-1200°C).

Figure 2(a) summarizes PL spectra of all the samples (A-I) grown at 1050 and 1200°C. The spectra are normalized by the absorbance at 405 nm. The spectra of samples grown at different temperatures are shown in the supporting information (Figure S1). Although the wavelength and the intensity are distributed depending on B and P concentrations, the spectra can be divided into two groups, *i.e.*, grown at 1050°C and 1200°C. Therefore, the growth temperature is a prime factor to determine the luminescence wavelength. However, even within the same growth temperature, the wavelength and the intensity are scattered. To scrutinize the effect of dopant concentration on the wavelength and the intensity, we plot them as a function of the B and P concentration for the samples grown at 1200°C in Figure 2(b). The symbols in the figure corresponds to the symbol in Table 1. Note that the concentration is that in Si-rich BPSG before annealing, which is not the same as that in Si QDs. The peak shifts to longer wavelength with increasing the B and P concentration. This is consistent with our previous work on B and P codoped Si QDs in BPSG matrices.[26] The dependence of the intensity is slightly different from that of the wavelength. The intensity is the largest in sample C and goes down to all directions. Similar dependence is observed for the samples grown at different temperatures (Figure S2 in the Supporting Information).

Figure 2(c) summarizes the PL QY of all the samples as a function of the PL peak wavelength. The ordinate is a logarithmic scale. The overall trend of the dependence is very similar to that reported in intrinsic Si QDs.[21,40–42] It has the maximum around 750 nm and goes down to both directions. Due to B and P codoping, the peak wavelength is extended to 1200 nm. The highest QY at NIR-I is 20.1% at 727 nm. Although this value is not very high compared to organic-capped Si QDs in non-polar solvents[21] and those in polymer,[43] it is to our best knowledge the highest in all-inorganic Si QDs in polar solvents in the NIR-I window. In the NIR-II window, the highest QY is 1.74% at 1052 nm. This value is much larger than that of typical water soluble fluorescence dye in the wavelength range and is again the highest QY in Si-based nanomaterial in polar solvents in the NIR-II window.

Figure 2(d) shows the PL lifetime as a function of the detection wavelength for samples A and C grown at different temperatures (1050-1200°C). Interestingly, in each series of sample, the lifetime trend is almost on a single curve irrespective of the growth temperature. The lifetime of sample C is always longer than that of sample A, especially in the NIR-II window. Figure 2(d) indicates that the quality of codoped Si QDs is primary determined by the composition of initial Si-rich BPSG and the primary role of the growth temperature is to determine the wavelength. All the results in Figure 2 suggest that impurities are doped not only in the substitutional sites but also in other sites and induce nonradiative processes. A possible nonradiative recombination site is three-coordinate B residing at Si QD surface.[44] The three-coordinate B traps an photoexcited electron and leaves a hole in a Si QD, which kills the luminescence via a three-body Auger recombination process.[45,46] We speculate that the density of the surface three-coordinate B atoms depends on the composition of initial Si-rich BPSG and thus the PL QY and the lifetime are determined by the composition.

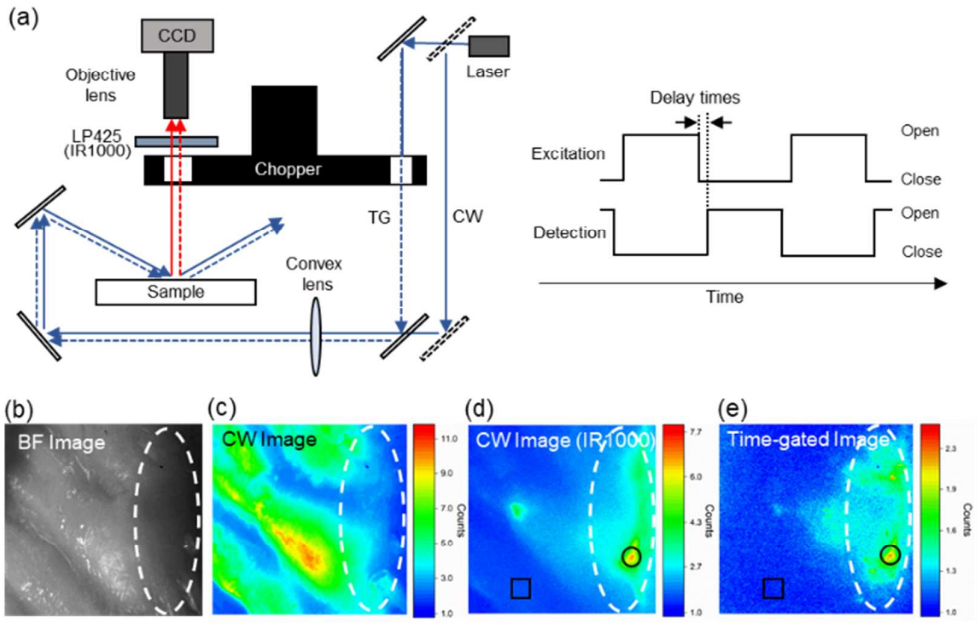

Figure 3. (a) Experimental setup for fluorescence imaging in the NIR-II region by using a mechanical chopper. For time-gated imaging, the excitation light is brought to the sample through an opening of a mechanical chopper, and the PL is brought to a conventional CCD camera through a different opening of the chopper. Due to asymmetric shape of the two openings, the PL detection starts after blocking off the excitation light as shown in the timing chart. (b) Bright field image of a chicken wing without laser excitation. A solution of Si QDs is injected in the region surrounded by a dashed circle. (c,d) Fluorescence images excited at 405 nm with 425 nm long pass filter (c) and with 1000 nm long pass filter (d) without time delay (CW). (e) Time-gated fluorescence image without 1000 nm long pass filter. The delay time is 128 µs. All images are taken at the same region.

In sample C, the lifetime exceeds 200 µs in the NIR-II window. This is to our best knowledge the longest luminescence lifetime of water-soluble phosphors in the wavelength range. Thanks to the very long lifetime, codoped Si QDs can be used for time-gated imaging in the NIR-II window, where a nanosecond-order high speed camera is not easily available. Figure 3(a) shows a setup for time-gated fluorescence imaging by using a mechanical chopper and a conventional CCD camera (ORCA-R^2, Hamamatsu Photonics). The excitation light (405 nm) is brought to the sample through an opening of a mechanical chopper, and the PL from a sample is detected by a CCD camera through a different opening of the same chopper. The excitation power is 1.47 mW/cm^2. Due to the asymmetric shape of the two openings, the PL detection starts after blocking off the excitation light as shown in the time chart in Figure 3(a). When the rotation speed of the chopper is 3900 rpm, the delay time is 128 µs, which is long enough to remove cell autofluorescence (several ns)[47], but still short enough to detect PL from codoped Si QDs. The validity of the setup is confirmed by observing time-gated imaging of Si QDs (C-1200) and Rhodamine B (RhB) on flat silica substrates in the same field (Figure S3 in the Supporting Information).

For the demonstration of time-gated imaging, colloidal solution of codoped Si QD (50 µl, Si QD concentration: 0.12 mg/ml) was subcutaneously injected into chicken wing. Figure 3(b) is the bright field image obtained under room light (no laser excitation). Si QDs are injected in the region surrounded by a dashed circle. Figure 3(c) is the fluorescence image without time-gating. The excitation light is removed by a 425 nm long-pass filter (LP425). Due to the strong autofluorescence, emission from Si QDs is not distinguished. In Figure 3(d), emission in the visible and NIR-I regions is removed by a long-pass filter (cutoff wavelength: 1000 nm) (IR1000). Autofluorescence is almost completely removed and emission from Si QDs can clearly be seen in the region surround by a dashed circle. Figure 3(e) shows a time-gated image of the same region. The IR1000 long-pass filter is removed and thus all the emission above 425 nm is collected. Due to very long luminescence lifetime of codoped Si QDs, a high contrast image is obtained without the filter. In Figure 3(d), the signal / background ratio is 8.4 and in Figure 3(e), it is 3.9. The contrast of the time-gated imaging can be improved by decreasing the delay time.

Conclusions

The relation between the PL wavelength, lifetime and QY of a colloidal solution of B and P codoped Si QDs and the composition of the starting material for the preparation was studied in detail. It was found that the PL lifetime and the QY are primarily determined by the composition, while the PL wavelength is mainly determined by the growth temperature. By optimizing the composition, we could achieve the QYs of 20.1 % and 1.74 % in NIR-I and NIR-II regions, respectively, in methanol for bare codoped Si QDs without organic ligands. We could also achieve over 200 µs PL lifetime in the NIR-II region.

We demonstrated time-gated imaging in the NIR-II range by using a codoped Si QDs phosphor.

Acknowledgements

This work was partly supported by the 2015 JST Visegrad Group (V4)−Japan Joint Research Project on Advanced Materials and JSPS KAKENHI Grant Number 16H03828 and 18K14092.

Notes and references

1 G. Hong, A. L. Antaris and H. Dai, *Nat. Biomed. Eng.*, 2017, **1**, 0010.
2 I. Yang, J. W. Lee, S. Hwang, J. E. Lee, E. Lim, J. Lee, D. Hwang, C. H. Kim, Y. S. Keum and S. K. Kim, *J. Photochem. Photobiol. B Biol.*, 2017, **166**, 52–57.
3 H. L. D. Lee, S. J. Lord, S. Iwanaga, K. Zhan, H. Xie, J. C. Williams, H. Wang, G. R. Bowman, E. D. Goley, L. Shapiro, R. J. Twieg, J. Rao and W. E. Moerner, *J. Am. Chem. Soc.*, 2010, **132**, 15099–15101.
4 S. Luo, E. Zhang, Y. Su, T. Cheng and C. Shi, *Biomaterials*, 2011, **32**, 7127–7138.
5 M. Heilemann, S. Van De Linde, M. Schüttpelz, R. Kasper, B. Seefeldt, A. Mukherjee, P. Tinnefeld and M. Sauer, 2008, 6172–6176.
6 M. Chalfie, Y. Tu, G. Euskirchen, W. Ward and D. Prasher, *Science (80-.).*, 1994, **263**, 802–805.
7 K. Welsher, S. P. Sherlock and H. Dai, *Proc. Natl. Acad. Sci.*, 2011, **108**, 8943–8948.
8 A. L. Antaris, H. Chen, K. Cheng, Y. Sun, G. Hong, C. Qu, S. Diao, Z. Deng, X. Hu, B. Zhang, X. Zhang, O. K. Yaghi, Z. R. Alamparambil, X. Hong, Z. Cheng and H. Dai, *Nat. Mater.*, 2016, **15**, 235–242.
9 A. L. Antaris, H. Chen, S. Diao, Z. Ma, Z. Zhang, S. Zhu, J. Wang, A. X. Lozano, Q. Fan, L. Chew, M. Zhu, K. Cheng, X. Hong, H. Dai and Z. Cheng, *Nat. Commun.*, 2017, **8**, 1–11.
10 X. Michalet, S. S. Gambhir and S. Weiss, *Science (80-.).*, 2005, **307**, 538–544.
11 Y. Kong, J. Chen, H. Fang, G. Heath, Y. Wo, W. Wang, Y. Li, Y. Guo, S. D. Evans, S. Chen and D. Zhou, *Chem. Mater.*, 2016, **28**, 3041–3050.
12 A. Sasaki, Y. Tsukasaki, A. Komatsuzaki, T. Sakata, H. Yasuda and T. Jin, *Nanoscale*, 2015, **7**, 5115–5119.
13 W. C. W. Chan and S. Nie, *Adv. Sci.*, 2009, **281**, 2016–2018.
14 X. Gao, Y. Cui, R. M. Levenson, L. W. K. Chung and S. Nie, *Nat. Biotechnol.*, 2004, **22**, 969–976.
15 Y. Zhang, G. Hong, Y. Zhang, G. Chen, F. Li, H. Dai and Q. Wang, *ACS Nano*, 2012, **6**, 3695–3702.
16 B. Dong, C. Li, G. Chen, Y. Zhang, Y. Zhang, M. Deng and Q. Wang, *Chem. Mater.*, 2013, **25**, 2503–2509.
17 A. Zebibula, N. Alifu, L. Xia, C. Sun, X. Yu, D. Xue, L. Liu, G. Li and J. Qian, *Adv. Funct. Mater.*, 2018, **28**, 1–13.
18 G. Chen, F. Tian, Y. Zhang, Y. Zhang, C. Li and Q. Wang, *Adv. Funct. Mater.*, 2014, **24**, 2481–2488.
19 F. Peng, Y. Su, Y. Zhong, C. Fan, S. T. Lee and Y. He, *Acc. Chem. Res.*, 2014, **47**, 612–623.
20 F. Erogbogbo, K. Yong, I. Roy, G. Xu, P. N. Prasad and M. T. Swihart, *ACS Nano*, 2008, **2**, 873–878.
21 F. Sangghaleh, I. Sychugov, Z. Yang, J. G. C. Veinot and J. Linnros, *ACS Nano*, 2015, **9**, 7097–7104.
22 M. H. Mobarok, T. K. Purkait, M. A. Islam, M. Miskolzie and J. G. C. Veinot, *Angew. Chemie - Int. Ed.*, 2017, **56**, 6073–6077.
23 B. F. P. McVey and R. D. Tilley, *Acc. Chem. Res.*, 2014, **47**, 3045–3051.
24 F. Erogbogbo, C. A. Tien, C. W. Chang, K. T. Yong, W. C. Law, H. Ding, I. Roy, M. T. Swihart and P. N. Prasad, *Bioconjug. Chem.*, 2011, **22**, 1081–1088.
25 S. Takeoka, M. Fujii and S. Hayashi, *Phys. Rev. B - Condens. Matter Mater. Phys.*, 2000, **62**, 16820–16825.
26 M. Fujii, K. Toshikiyo, Y. Takase, Y. Yamaguchi and S. Hayashi, *J. Appl. Phys.*, 2003, **94**, 1990–1995.
27 Y. Hori, S. Kano, H. Sugimoto, K. Imakita and M. Fujii, *Nano Lett.*, 2016, **16**, 2615–2620.
28 O. Ashkenazi, D. Azulay, I. Balberg, S. Kano, H. Sugimoto, M. Fujii and O. Millo, *Nanoscale*, 2017, 17884–17892.
29 H. Sugimoto, M. Fujii, K. Imakita, S. Hayashi and K. Akamatsu, *J. Phys. Chem. C*, 2013, **117**, 11850–11857.
30 H. Sugimoto, M. Fujii, K. Imakita, S. Hayashi and K. Akamatsu, *J. Phys. Chem. C*, 2012, **116**, 17969–17974.
31 H. Sugimoto, M. Fujii, Y. Fukuda, K. Imakita and K. Akamatsu, *Nanoscale*, 2014, **6**, 122–6.
32 H. Sugimoto, M. Fujii, K. Imakita, S. Hayashi and K. Akamatsu, *J. Phys. Chem. C*, 2013, **117**, 6807–6813.
33 H. Sugimoto, M. Yamamura, M. Sakiyama and M. Fujii, *Nanoscale*, 2018, **10**, 7357–7362.
34 L. Ostrovska, A. Broz, A. Fucikova, T. Belinova, H. Sugimoto, T. Kanno, M. Fujii, J. Valenta and M. H. Kalbacova, *RSC Adv.*, 2016, **6**, 63403–63413.
35 T. Belinova, L. Vrabcova, I. Machova, A. Fucikova, J. Valenta, H. Sugimoto, M. Fujii and M. Hubalek Kalbacova, *Phys. Status Solidi*, 2018, **1700597**, 1700597.
36 J. Joo, X. Liu, V. R. Kotamraju, E. Ruoslahti, Y. Nam and M. J. Sailor, *ACS Nano*, 2015, **9**, 6233–6241.
37 L. Gu, D. J. Hall, Z. Qin, E. Anglin, J. Joo, D. J. Mooney, S. B. Howell and M. J. Sailor, *Nat. Commun.*, 2013, **4**, 1–7.
38 O. E. Semonin, J. C. Johnson, J. M. Luther, A. G. Midgett, A. J. Nozik and M. C. Beard, *J. Phys. Chem. Lett.*, 2010, **1**, 2445–2450.
39 H. J. Yvon, A guide to recording Fluorescence Quantum Yields, http://www.horiba.com/fileadmin/uploads/Scientific/Documents/Fluorescence/quantumyieldstrad.pdf.
40 X. Liu, Y. Zhang, T. Yu, X. Qiao, R. Gresback, X. Pi and D. Yang, *Part. Part. Syst. Charact.*, 2015, n/a--n/a.
41 C. M. Hessel, D. Reid, M. G. Panthani, M. R. Rasch, B. W. Goodfellow, J. Wei, H. Fujii, V. Akhavan and B. A. Korgel, *Chem. Mater.*, 2012, **24**, 393–401.
42 D. C. Hannah, J. Yang, P. Podsiadlo, M. K. Y. Chan, A. Demortière, D. J. Gosztola, V. B. Prakapenka, G. C. Schatz, U. Kortshagen and R. D. Schaller, *Nano Lett.*, 2012, **12**, 4200–4205.
43 A. Marinins, R. Zandi Shafagh, W. Van Der Wijngaart, T. Haraldsson, J. Linnros, J. G. C. Veinot, S. Popov and I. Sychugov, *ACS Appl. Mater. Interfaces*, 2017, **9**, 30267–30272.

44 L. M. Wheeler, N. J. Kramer and U. R. Kortshagen, *Nano Lett.*, 2018, **18**, 1888–1895.
45 A. Mimura, M. Fujii, S. Hayashi and K. Yamamoto, 1999, **109**, 561–565.
46 M. Fujii, S. Hayashi and K. Yamamoto, *J. Appl. Phys.*, 1998, **83**, 7953–7957.
47 M. M. Y. Berezin and S. Achilefu, *Chem. Rev.*, 2010, **110**, 2641–84.